ACS OMEGA

Open Access

http://pubs.acs.org/journal/acsodf

Article

Understanding the Resistive Switching Behaviors of Top Electrode (Au, Cu, and Al)-Dependent TiO_2-Based Memristive Devices

Yantao Yu, Zizhao Ding, Yaoying Ren, Xiangfei Wang, Hongguang Quan, Hong Jia,* and Chao Jiang*

Cite This: *ACS Omega* 2024, 9, 24601−24609

Read Online

ACCESS | Metrics & More | Article Recommendations | Supporting Information

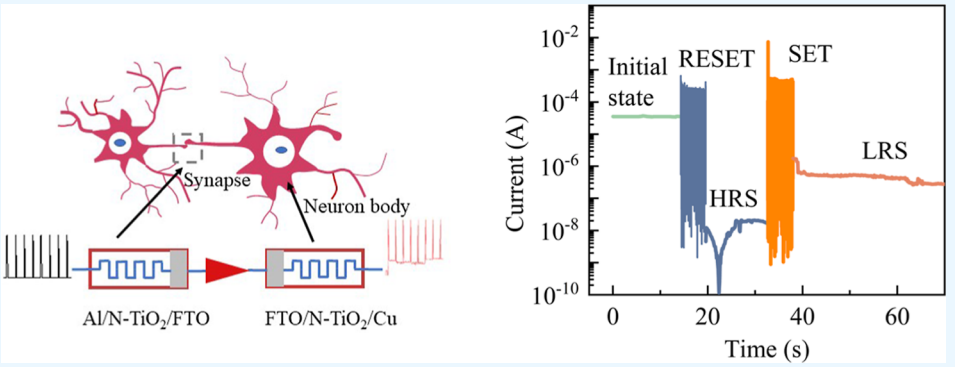

ABSTRACT: Memristor-based neuromorphic computing is promising toward their potential application of handling complex parallel tasks in the period of big data. To implement brain-inspired applications of spiking neural networks, new physical architecture designs are needed. Here, a serial memristive structure (SMS) consisting of memristive devices with different top electrodes is proposed. Top electrodes Au, Cu, and Al are selected for nitrogen-doped TiO_2 nanorod array-based memristive devices. The typical $I-V$ cycles, retention, on/off ratio, and variations of cycle to cycle of top electrode-dependent memristive devices have been studied. Devices with Cu and Al electrodes exhibit a retention of over 10^4 s. And the resistance states of the device with the Al top electrode are reliable. Furthermore, the conductive mechanism underlining the $I-V$ curves is discussed in detail. The interface-type mechanism and block conductance mechanism are illustrated, which are related to electron migration and ion/anion migration, respectively. Finally, the SMS has been constructed using memristive devices with Al and Cu top electrodes, which can mimic the spiking pulse-dependent plasticity of a synapse and a neuron body. The SMS provides a new approach to implement a fundamental physical unit for neuromorphic computing.

1. INTRODUCTION

Concerning the energy consumption and computing efficient especially, computing for complex issues is still a challenging task.[1] Neuromorphic computing is believed to break down the bottleneck in a conventional computing system.[2] In contrast to early artificial neural networks (ANNs) and deep neural networks, spiking neural networks (SNNs) are proposed to meet acceptable energy efficiency, which has a highly biological realizability.[3−5] Nevertheless, the SNNs have not been successful commercially for lacking reliable devices and fundamental architecture.[6] Generally, a SNN unit physically needs to show spiking plasticity and memory. Nowadays, researchers have paid much attention to realizing synaptic behaviors by utilizing a single device.[7] However, a delicate design unit which can conduct spiking plasticity and memory separately is also a strong need.[8] In fact, biological behaviors originating from the synapses, dendrites, and soma can be integrated together to design brain-like devices.[9] In previous studies, most researchers focused on simulating a portion of the neuron rather than the entire nerve. Concerning electronic synapses, the migration of oxygen vacancies in TiO_2-based memristors has been successfully utilized to perform synaptic behaviors.[10] Metal Ag nanoclusters embedded in TiO_2-based memristors are also used to achieve continuously changed conductance for mimicking electronic synapses.[11] As we already know, dendrites are also important in human cortical neurons.[12] Yang has mimicked dendrites using several parallel memristors, which actually collect the accumulated current of memristors caused by an external stimulus.[8] As for soma, Alaaddin has compared Ag contact- and Au contact-based memristors in terms of the capability of storage charge.[13] In further, it is reported that nonvolatile memristive devices with

Received: January 24, 2024
Revised: April 26, 2024
Accepted: April 30, 2024
Published: May 26, 2024

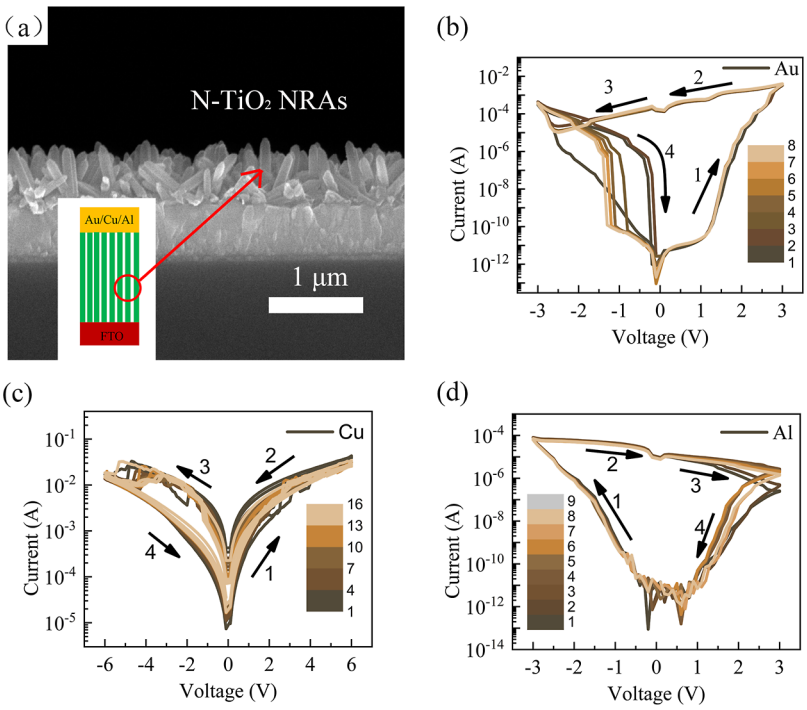

Figure 1. (a) Cross-sectional image for N−TiO_2 NRAs (inset: schematic structure of fabricated devices). The *I*−*V* characteristics for N−TiO_2 NRAs/FTO-based memristive devices with top electrodes (b) Au, (c) Cu, and (d) Al, respectively.

a TiO_2 layer have exhibited reliable memory feature for SNNs,[14,15] while volatile memristive devices have been proved to mimic pulse activities in the human brain, which can relax to its normal resistance state spontaneously.[16,17] Chen has successfully built ANNs using the Au top electrode in hexagonal boron nitride based memristors, and the research further indicates applications of SNNs by using the Ag top electrode which showed multilevel conductance, lower energy consumption, and stable relaxation.[18] From the sight of memristor structure design, electrodes play an important role to realize various resistive switching behaviors and enhance the properties of memristive devices.[17,19−23] The inert metal Au can regulate the concentration of oxygen vacancies by forming an interface potential barrier, and the active metal (Cu and Al) can regulate the conductive states by forming metallic filaments.[24−27] Hence, it is feasible to achieve multibiological behaviors in TiO_2-based memristive devices by designing metal electrodes. A serial memristive structure (SMS) composed of electrode-dependent devices is a promising method to implement SNNs physically.[28,29] The mechanism and reliability of electrode-dependent devices need to be studied systematically.[14,30,31]

In this work, we investigate the effect of electrodes (Au, Cu, and Al) on the memristive behaviors of TiO_2-based devices, and a SMS has been proposed to perform spiking events for SNNs successfully. The SMS consists of two memristors with different top electrodes, which mimic a synapse and a neuro body, respectively. This SMS demonstrates a promising approach to implement physical SNNs using feasible manufacturing processes.

2. EXPERIMENTAL SECTION

The memristive layer of nitrogen-doped TiO_2 nanorod arrays (N−TiO_2 NRAs) is grown on fluorine-doped tin oxide (FTO, manufactured by Aasahi Glass Co., Ltd.) by a hydrothermal process as described in prior works.[32] Top electrodes Au, Cu, and Al (target purity, 99.99%) are deposited using a magnetic sputtering process. Metal atoms cover the nanorods well because the surface of N−TiO_2 NRAs is rough. The layer thickness of the electrodes is about 80−100 nm measured by field emission scanning electron microscopy (SEM, Nova Nano SEM230). The SMS is constructed with memristive devices configurating a Cu electrode and an Al electrode. A silver wire of about 10 μm diameter and an indium patch were used to connect two bottom electrodes (FTO substrates) of two memristive devices. A certain length of the silver wire was placed on the FTO substrates. Then, a small bulk of indium was cut and placed on one terminal of the silver wire. Finally, the indium bulk was pressed carefully to form a patch and fix the wire well. The contact resistance between the silver wire and FTO is less than 70 Ω. The electrical tests have been finished using an Agilent B1500A semiconductor (Agilent Inc., Santa Clara, CA, USA). For the cycle measurement, FTO served as the bottom electrode, and the step length of the applied voltage was set at 0.1 V. A probing station was used to connect the devices. For the SMS, the Al electrode served as the top electrode, and the Cu electrode was grounded. And FTO served as a middle electrode, which can be used to operate either device. A series of spiking pulses were implemented by a WGFMU pattern, and read operations were finished using the *i*−*t* sample model. All of the measurements were carried out in air atmosphere and at room temperature.

3. RESULTS AND DISCUSSION

Figure 1 shows the SEM image of fabricated N−TiO_2 NRAs and cycle-to-cycle performances of memristive devices with Au, Cu and Al electrodes. All the three devices show good bipolar resistive switching behaviors, which demonstrate a significant window of *I*−*V* loops. The devices with Au and Cu top

https://doi.org/10.1021/acsomega.4c00320
ACS Omega 2024, 9, 24601−24609

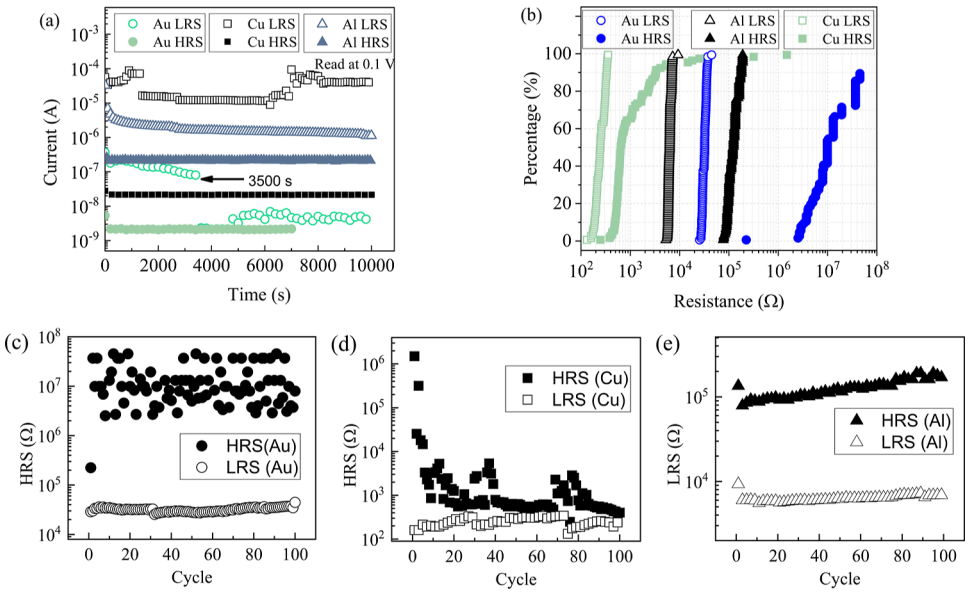

Figure 2. (a) Retention of HRS and LRS in devices with different top electrodes. (b) CPD of HRS and LRS during 100 cycles in devices with different top electrodes. The changes of HRS and LRS with increasing cycles in devices with (c) Au, (d) Cu, and (e) Al top electrodes.

electrodes change from high-resistance state (HRS) to low-resistance state (LRS) under positive bias, while the device with the Al top electrode changes to LRS by negative bias. As the functional layers of N−TiO_2 NRAs in these devices are the same, the difference of polars of resistive switching is believed to be caused by the interface effects of M/N−TiO_2 NRAs (M = Au, Cu, and Al). The effects related to electrodes will be discussed in the latter parts. Concerning the window area of *I*−*V* loops, the device with the Au top electrode has the biggest window area, while the device with the Cu top electrode has the smallest window area. During the set processes, the devices with Au and Al top electrodes exhibit threshold value feature, which has been generally attributed to Schottky effects.[33] This threshold feature can be utilized to suppress dark current or implement trigger function of spiking pulses.[34] During the set process and reset process of the device with the Cu top electrode, the response current changed dramatically. It is explained that metal filaments composed of Cu^{2+} ions have formed during resistive switching processes. And the formation and fusion of Cu filaments led to the dramatic changes of current.[35] The response current for the Al top electrode device gradually changed during the *I*−*V* cycles, which is attributed to the influence of interface barrier potential on the continuous drift process of oxygen vacancies.[36]

Figure 2 shows the retention and distribution of HRS and LRS for devices with Au, Cu, and Al top electrodes. The retention of 10^4 s in Figure 1a was read after a set or reset operation. The curves of cumulative probability distribution (CPD) of HRS and LRS in Figure 2b have been obtained by abstracting data from 100 *I*−*V* cycles (as shown in Figure S1). As can be seen in Figure 2a, the devices with Cu and Al electrodes exhibit a stable ratio of HRS/LRS, while that feature for the device with the Au top electrode degrades gradually and eventually shrinks to a failure level after 3500 s. It is noticed that two drastic fluctuations occurred for the retention of LRS of the Cu top electrode device, which could be caused by diffusion of accumulated Cu atmos. The conductive filaments composed of Cu within the N−TiO_2 NRA medium are susceptible to interference even with small read bias.[24] The HRS/LRS ratios are over 10 for devices of Al and Cu top electrodes range of 10^4 s, which is acceptable for devices to mimic short-term memory and long-term memory.[37−39] Figure 2b shows the CPD of HRS and LRS during 100 consecutive cycles for the studied devices. The resistance states of devices with Au and Cu top electrodes show obvious variations, as shown in Figure 2c,d. In contrast, the device with an Al electrode exhibits small variation and better stability in Figure 2e. The 100 *I*−*V* cycles of the devices can be seen in Figure S1. The coefficient of variation (COV) has been used to estimate the fluctuation of resistance states, which is defined as the standard deviation (σ) divided by the mean value (μ). In further, the device-to-device uniformity of Al top electrodes is shown in Figure S2. All COV values of HRS and LRS during cycles for studied devices are listed in Table 1. A reason for the

Table 1. COV of Cycle to Cycle for Devices with Au, Cu, and Al Top Electrodes

	coefficient of variation (σ/μ)	
top electrode used in devices	LRS	HRS
Au	0.0966	2.7316
Cu	0.2255	0.5531
Al	0.0749	0.2390

variations could be that the conductive filaments consisting of high concentration of metal atoms or oxygen vacancies are particularly unstable after cycling.[40] The accumulated V_o (oxygen vacancies) could be a reason for the fluctuation of HRS in devices with a Au top electrode. The Cu^{2+} cations will accumulate in the TiO_2 medium which induces the HRS of the device to degrade to LRS (as shown in Figures 2c and S1b). The HRS and LRS of the device with the Al top electrode show minor variation.

To understand the resistive switching process, the *I*−*V* profiles have been fitted using Schottky emission, Poole−Frankel (P−F) emission, space charge limited current (SCLC), and Fowler−Nordheim (F−N) tunneling conductive mechanisms, systematically.[41,42] Figure 3 shows the matched

https://doi.org/10.1021/acsomega.4c00320
ACS Omega 2024, 9, 24601−24609

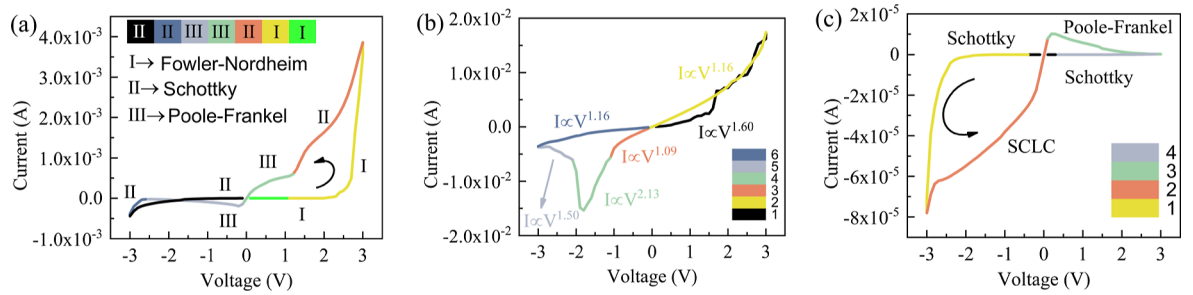

Figure 3. Conductive mechanisms in different regions of the single $I-V$ loop in memristive devices with (a) Au, (b) Cu, and (c) Al top electrodes.

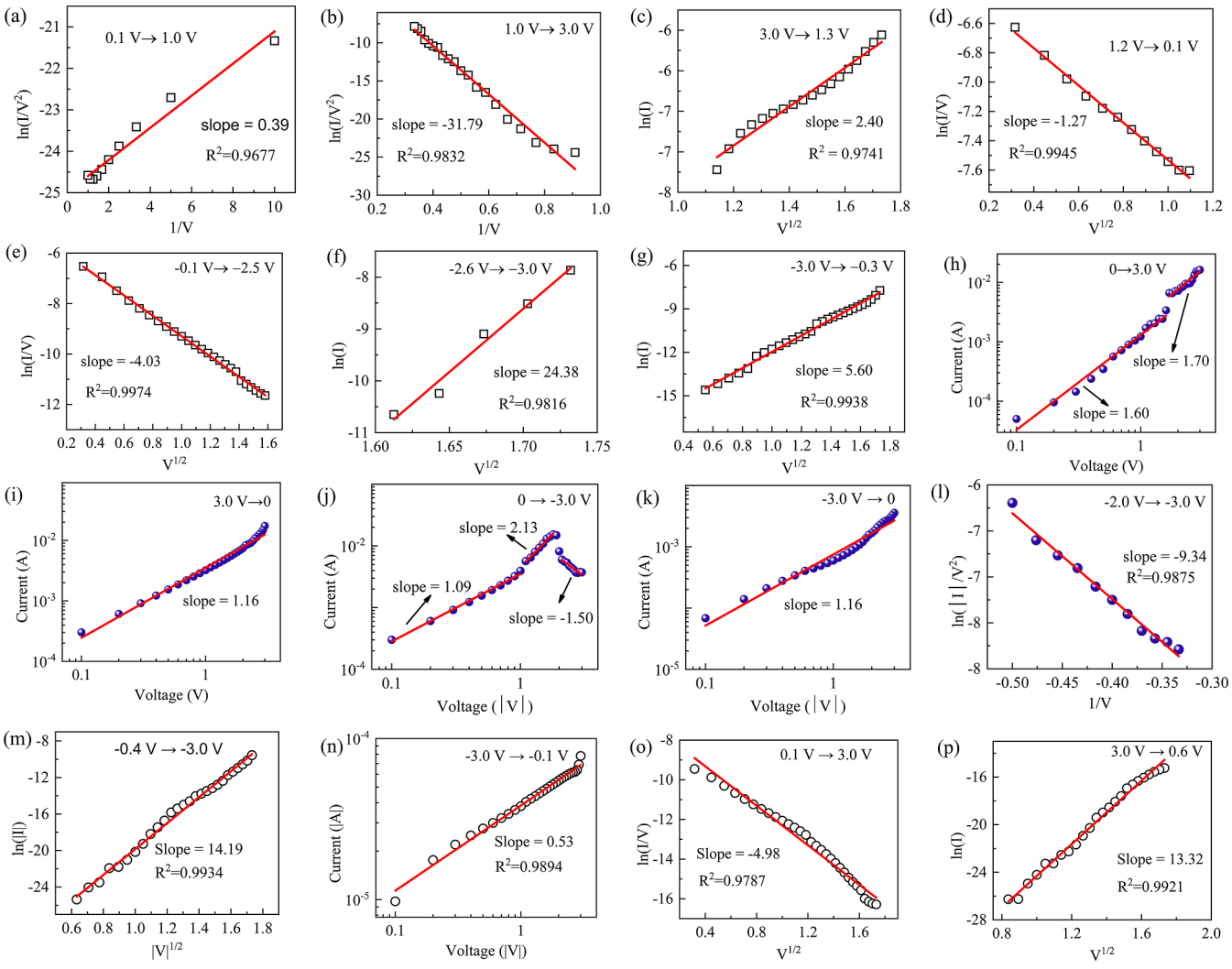

Figure 4. Linear fitting of conductive mechanisms for devices of (a–g) Au/N–TiO_2 NRAs/FTO, (h–l) Cu/N–TiO_2 NRAs/FTO, and (m–p) Al/N–TiO_2 NRAs/FTO.

conductive mechanisms for various regions during the cycles. And the details of linear fitting are shown in Figure 4. During one cycle of $I-V$, there could exist more than one conductive mechanism. The coefficient of determination (COD) of linear fitting was used to determine which mechanisms dominate the resistive switching process and explain the $I-V$ curve well in this work. The COD values (R^2) that can be obtained from the linear fit using Origin software were compared. The detailed R^2 of each region of the $I-V$ curves can be seen in Tables S1–S3. For the device with a Au top electrode, F–N tunneling, Schottky emission, and P–F emission mechanisms are fitted well with different regions of the $I-V$ curves. In positive regions, when the sweeping voltage increases from 0 to 3 V, the current is dominated by the F–N mechanism. This mechanism can also be seen in devices with electrodes of high work function, such as Pt and C.[43] It is agreed that a potential barrier exists at the interface of M/N–TiO_2 NRAs, which can be narrowed due to the insertion of oxygen vacancies. Electrons can tunnel through the barrier under enough voltage bias. With the sweeping voltage applied, oxygen vacancies will accumulate at the interface. Then, when the applied voltage decreases to a low level (the region of the green color line in Figure 3a), the

https://doi.org/10.1021/acsomega.4c00320
ACS Omega 2024, 9, 24601–24609

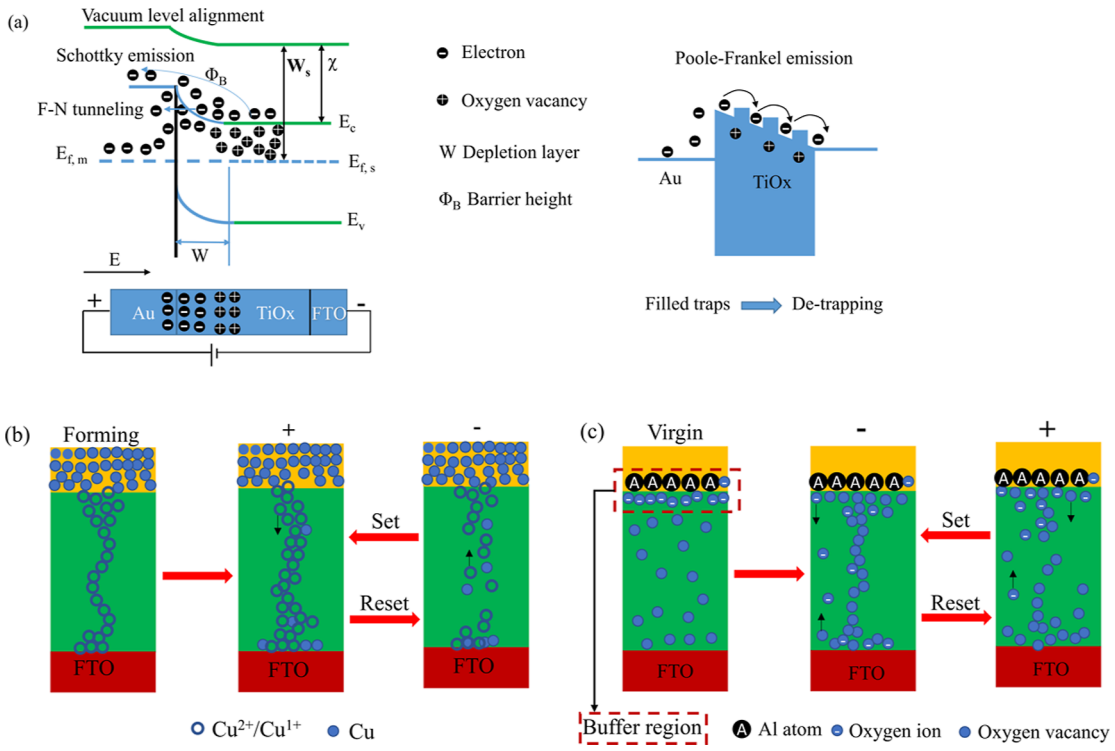

Figure 5. Schematics of main mechanisms corresponding to devices with different electrodes. (a) Interface and block-type electron transportation dependent on the Au electrode; (b) formation and disconnection of metal filaments dependent on the Cu electrode; and (c) bridging and rupture of filaments of oxygen vacancies dependent on the Al electrode.

curve is fitted well by the P−F emission mechanism (shown in Figure 4d). It can be explained that plenty of vacancies released due to the concentration gradient. When the bias reverses and is at a low level, the device is still dominated first by the P−F emission mechanism (shown in Figure 4e). When the reverse bias increases from −2.6 to −3.0 V and then sweeps from −3.0 to −0.3 V, the Schottky emission mechanism dominates the current (shown in Figure 4f,g). It is concluded that the interface effect plays an important role in the device with the Au electrode.

For the device with a Cu top electrode, the *I*−*V* curve can be fitted by the SCLC mechanism successfully as shown in Figure 4h−l. During the set process of sweeping voltage from 0 to 3.0 V, the fitted slopes (log *I* vs log *V*) are 1.60 and 1.70 as shown in Figure 4h, while the fitted slopes are 2.13 and −1.50 during the reset process as shown in Figure 4j, respectively. It is verified that the set process is in accordance with SCLC ($I \propto V^n$).[42] When the device is at LRS and HRS states in Figure 4i,k, the fitted slopes of *I*−*V* are both nearly 1.00, which indicated an ohmic conductive mechanism. The Cu electrode has a lower work function than TiO_2,[44] so the interface effect has little contribution to the conductance of Cu electrode-based devices. Under positive bias, Cu^{2+} ions can migrate from the top electrode to N−TiO_2 NRAs and can residue in the medium as isolated Cu isles. And in this case, Cu ions became the major carriers and induced to form a space charge region.

The *I*−*V* curve of the device with the Al top electrode shown in Figure 3c has been fitted well with the Schottky emission, SCLC, and P−F emission. The device can be set to a LRS with negative bias and be reset to a HRS with positive bias. The set process can be fitted by the Schottky emission mechanism as shown in Figure 4m. When the device is at LRS, the *I*−*V* curve has been fitted well by the SCLC mechanism shown in Figure 4n, and the fitted slope of 0.53 indicated an Ohmic-like contact. During the reset process, P−F emission dominated the conductance as fitted in Figure 4o, which is caused by the detrapping process of oxygen vacancies. When the detrapping process completed, the device changed to its HRS. When the device is at HRS, the *I*−*V* is dominated by the Schottky emission mechanism as shown in Figure 4p. It is indicated that there is a potential barrier in the Al/N−TiO_2 interface. In conclusion, when the potential barrier (interface effects) or potential well (trapping/detrapping centers of oxygen vacancies) dominated the conductance of devices, the resistive switching behaviors exhibited gradual changing current. While the metallic conductive filament mechanisms dominated the resistive switching behaviors, drastic changing current was tended to appear.

Figure 5 illustrates the main mechanisms underlining the memristive behaviors in the three types of devices. It is revealed that three conductive mechanisms have dominated the whole memristive process in the Au/N−TiO_2 NRAs/FTO device. As shown in Figure 5a, the depletion layer starts to narrow down with forward bias applied; then, the electrons can tunnel the depletion layer. At the same time, the oxygen vacancies move from the Au top electrode to the FTO substrate, and electrons will fill the oxygen vacancy-based potential well gradually. When the forward bias decreases from 3.0 to 1.3 V, the F−N tunneling effect diminished, and the Schottky emission becomes a main mechanism. During the sweeping process from 1.2 to −2.5 V, the filled oxygen vacancies begin to detrap electrons, and the P−F emission becomes the main mechanism underlining the *I*−*V* behavior. As the filled oxygen vacancies changed their state to a virgin empty state, the device changed to HRS. Then, with backward bias increasing from −2.6 to −3.0 V, oxygen vacancies will

https://doi.org/10.1021/acsomega.4c00320
ACS Omega 2024, 9, 24601−24609

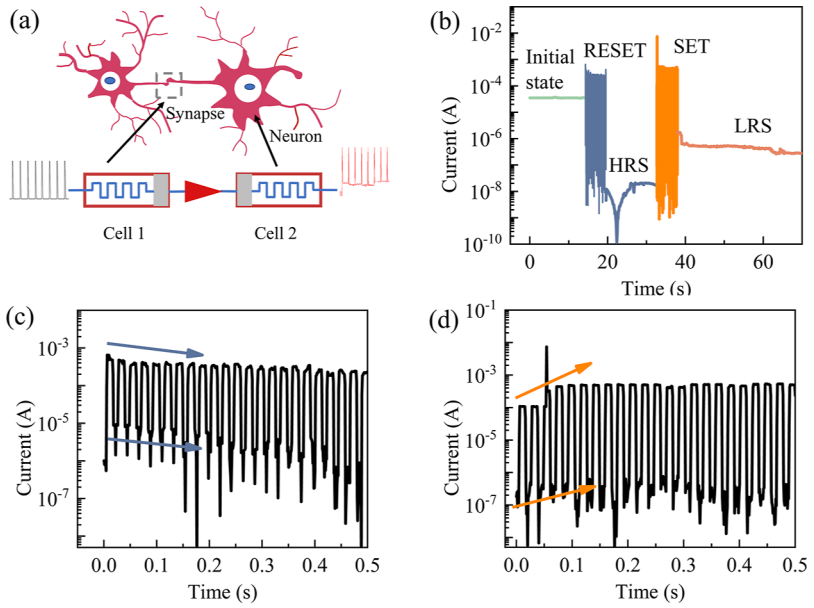

Figure 6. SMS and spiking pulse responses. (a) Schematic of a serial structure of biological neurons and a SMS of two devices physically, (b) set and reset process responding to spiking pulses, (c) depression current during the reset process in (b), and (d) potentiation current during the set process in (b).

accumulate at the Au/N−TiO_2 NRA interface, and an increasing current process occurs. It is explained that the thickness of the deplete layer related to the Schottky emission dominates the current. Because of the existence of the Schottky barrier, the current in the backward region from −3 to 0 V is relatively low. Figure 5b shows the formation and disconnection of metal filaments in the device with a Cu electrode. The electrochemical metallization process has been performed with active metal Cu.[24,45] With positive bias applied on the Cu top electrode, Cu atoms are oxidized as Cu^{2+} ions, and these ions will migrate toward the bottom electrode. A portion of Cu^{2+} ions was reduced to Cu atoms and occurred on the conductive pathway.[35] Before the conductive filaments of Cu atoms formed, an apparent gap existed between the top and bottom electrodes. So, the SCLC mechanism plays a dominant role during the set process.[46] After the Cu conductive filaments occurred with the set operation, the current following through the device was complied with Ohmic law. Figure 5c shows the bridging and rupture of filaments of oxygen vacancies in the Al electrode device. It is assumed that Al atoms are oxidized near the surface of the N−TiO_2 NRAs. And an ultrathin oxidized layer has been formed and serves as a buffer region. Al atoms are facilitated to be oxidized and are less possible to migrate under an applied voltage because Al^{3+} has less diameter than Cu^{2+} and the oxidation potential of Al (−1.660 V) is more negative than that of Cu (0.337 V).[47,48] The conductance of the Al electrode device is subject to the Al−O−Ti interface and the block of oxygen vacancies. When the device is set to LRS, the current is complied with the SCLC mechanism as the filaments of oxygen vacancies were bridging. The oxygen vacancies served as traps and can be filled with electrons. When the applied bias changed its polar direction, the trapped electrons escaped from the oxygen vacancy-based potential well.[41] Hence, the P−F emission mechanism plays a main role during the reset process.

As in human brain, a real neuron is composed of one body and one or more synapses.[8] The synapses take charge of collecting and amplifying signals from adjacent synapses. The neuronal body can record information and fire pulses. This fundamental structure is essential to inspire neuromorphic computing. Memristors with different electrodes can play specific roles in neuromorphic computing. Here, we use SMS as a fundamental unit for neuromorphic computing, which acts as one volatile memristive device and one nonvolatile memristive device. Figure 6 illustrates the schematic diagram of the proposed SMS and its response process to spiking stimuli. In Figure 6a, it is shown that the devices with Al and Cu electrodes serve as synapse (cell 1) and neuron body (cell 2), respectively. The serial structure can be described as Al/N−TiO_2/FTO/Ag/FTO/N−TiO_2/Cu. Cell 1 with the Al electrode can respond to the stimuli and change its weight, while cell 2 with the Cu electrode can record the strengthening of the stimuli. Figure 6b shows the changing current versus time with a set of pulses carried on the SMS, which included spiking number plasticity and retention of conductance. Figure 6c,d shows the current during the reset process and the set process in detail, respectively. Cell 2 (with the Cu electrode) has been set to LRS before the test. Then, with positive voltage pulses, cell 1 and cell 2 change to HRS. Then, with negative voltage pulses, the two cells switch to LRS. Gradually changed current can be observed during the first four pulses, which indicates that the SMS has the capability to mimic synaptic potentiation and depression behaviors using devices with different electrodes. The Cu electrode device and the Al electrode device in the SMS acted as one nonvolatile memristive device and one volatile device, respectively. As the SMS exhibits the ability to conduct and store biological electric signals, it paves a way to mimic synapses and neurons by using electrode-dependent memristive devices.

4. CONCLUSIONS

The resistive switching behaviors and conductive mechanisms for N−TiO_2 NRA-based memristive devices with Au, Cu, and Al top electrodes have been studied. The retentions for devices with Cu and Al top electrodes are over 10^4 s. The COV of LRS for the device with the Al top electrode is 0.0749. The

https://doi.org/10.1021/acsomega.4c00320
ACS Omega 2024, 9, 24601−24609

conductance is subject to interface and oxygen vacancy distribution in the Al/N−TiO_2 NRAs/FTO device, for which the Schottky emission dominates the HRS region, while the SCLC and P−F emission mechanisms dominate the LRS region. For Cu/N−TiO_2 NRAs/FTO devices, the SCLC mechanism explains the resistive switching behaviors well, which is related to the metallic filaments of Cu. A SMS of Al/N−TiO_2 NRAs/FTO/Ag/FTO/N−TiO_2 NRAs/Cu has been fabricated to perform spiking pulse plasticity, which mimics the transition and memory of pulse signals in the neurons of the human brain physically.

■ ASSOCIATED CONTENT

Supporting Information

The Supporting Information is available free of charge at https://pubs.acs.org/doi/10.1021/acsomega.4c00320.

100 consecutive $I-V$ cycles of devices of Au, Cu, and Al electrodes; device-to-device uniformity for devices with the Al top electrode; and correlation coefficient (R^2) of the fitting of different conductive mechanisms related to Au and Al top electrodes devices (PDF)

■ AUTHOR INFORMATION

Corresponding Authors

Hong Jia − *College of Physics and Electronic Information, Luoyang Normal University, Luoyang 471934, China*; Email: jiahong517@aliyun.com

Chao Jiang − *Powder Metallurgy Research Institute, Central South University, Changsha 410083, China*; orcid.org/0000-0001-6367-9936; Email: jiangchao@csu.edu.cn

Authors

Yantao Yu − *College of Physics and Electronic Information, Luoyang Normal University, Luoyang 471934, China*

Zizhao Ding − *Powder Metallurgy Research Institute, Central South University, Changsha 410083, China*

Yaoying Ren − *College of Physics and Electronic Information, Luoyang Normal University, Luoyang 471934, China*

Xiangfei Wang − *College of Physics and Electronic Information, Luoyang Normal University, Luoyang 471934, China*

Hongguang Quan − *College of Physics and Electronic Information, Luoyang Normal University, Luoyang 471934, China*

Complete contact information is available at: https://pubs.acs.org/10.1021/acsomega.4c00320

Author Contributions

Y. Yu proposed the conception and designed the experiments. Y. Yu, Y. Ren, and X. Wang performed the experiments. Z. Ding and H. Jia carried out the measurements. Y. Yu and C. Jiang wrote the manuscript. All authors contributed to the general discussion.

Notes

The authors declare no competing financial interest.

The authors declare that they have no conflict of interest and no living organisms were harmed.

■ ACKNOWLEDGMENTS

This work was supported in part by the Henan Provincial Science and Technology Research Project (grant no. 232102210180). This work was also supported in part by the Youth Backbone Teacher of Henan Province (2020GGJS197), the Natural Science Foundation of Henan Province (212300410375), the Key Scientific Research Projects of Henan Province (grant 21A140018), the College Students Innovations Special Project (grant nos. 202110482016, 202110482022, 202110482028, and 202210482004), the Science and Technology Plan Project of Hunan Province (grant no. 2015TP1007), the Young Scientific and Technological Innovation Talents in Hunan (grant no. 2021RC3003), the Significant Science and Technology Projects of LongMen Laboratory in Henan Province (grant no. 231100220100), and the Key Research and Development Program of Henan Province (grant no. 231111222200).

■ REFERENCES

(1) John, R. A.; Milozzi, A.; Tsarev, S.; Brönnimann, R.; Boehme, S. C.; Wu, E.; Shorubalko, I.; Kovalenko, M. V.; Ielmini, D. Ionic-electronic halide perovskite memdiodes enabling neuromorphic computing with a second-order complexity. *Sci. Adv.* **2022**, *8*, No. eade0072.

(2) Li, Z.; Tang, W.; Zhang, B.; Yang, R.; Miao, X. Emerging memristive neurons for neuromorphic computing and sensing. *Sci. Technol. Adv. Mater.* **2023**, *24*, 2188878.

(3) Zhou, G.; Wang, Z.; Sun, B.; Zhou, F.; Sun, L.; Zhao, H.; Hu, X.; Peng, X.; Yan, J.; Wang, H.; Wang, W.; Li, J.; Yan, B.; Kuang, D.; Wang, Y.; Wang, L.; Duan, S. Volatile and nonvolatile memristive devices for neuromorphic computing. *Adv. Electron. Mater.* **2022**, *8*, 2101127.

(4) Wang, Q.; Niu, G.; Ren, W.; Wang, R.; Chen, X.; Li, X.; Ye, Z. G.; Xie, Y. H.; Song, S.; Song, Z. Phase change random access memory for neuro-inspired computing. *Adv. Electron. Mater.* **2021**, *7*, 2001241.

(5) Sun, B.; Guo, T.; Zhou, G. D.; Ranjan, S.; Jiao, Y. X.; Wei, L.; Zhou, Y. N.; Wu, Y. A. Synaptic devices based neuromorphic computing applications in artificial intelligence. *Mater. Today Phys.* **2021**, *18*, 100393.

(6) Lee, C.; Sarwar, S. S.; Panda, P.; Srinivasan, G.; Roy, K. Enabling spike-based backpropagation for training deep neural network architectures. *Front. Neurosci.* **2020**, *14*, 497482.

(7) Demin, V. A.; Nekhaev, D. V.; Surazhevsky, I. A.; Nikiruy, K. E.; Emelyanov, A. V.; Nikolaev, S. N.; Rylkov, V. V.; Kovalchuk, M. V. Necessary conditions for stdp-based pattern recognition learning in a memristive spiking neural network. *Neural Network.* **2021**, *134*, 64−75.

(8) Yang, R.; Huang, H.-M.; Hong, Q.-H.; Yin, X.-B.; Tan, Z.-H.; Shi, T.; Zhou, Y.-X.; Miao, X.-S.; Wang, X.-P.; Mi, S.-B.; Jia, C.-L.; Guo, X. Synaptic suppression triplet-stdp learning rule realized in second-order memristors. *Adv. Funct. Mater.* **2018**, *28*, 1704455.

(9) Li, X.; Tang, J.; Zhang, Q.; Gao, B.; Yang, J. J.; Song, S.; Wu, W.; Zhang, W.; Yao, P.; Deng, N.; Deng, L.; Xie, Y.; Qian, H.; Wu, H. Power-efficient neural network with artificial dendrites. *Nat. Nanotechnol.* **2020**, *15*, 776−782.

(10) Park, J.; Park, E.; Kim, S.; Yu, H.-Y. Nitrogen-induced enhancement of synaptic weight reliability in titanium oxide-based resistive artificial synapse and demonstration of the reliability effect on the neuromorphic system. *ACS Appl. Mater. Interfaces* **2019**, *11*, 32178−32185.

(11) Yan, X.; Zhao, J.; Liu, S.; Zhou, Z.; Liu, Q.; Chen, J.; Liu, X. Y. Memristor with Ag-cluster-doped TiO_2 films as artificial synapse for neuroinspired computing. *Adv. Funct. Mater.* **2018**, *28*, 1705320.

(12) Marković, D.; Mizrahi, A.; Querlioz, D.; Grollier, J. Physics for neuromorphic computing. *Nat. Rev. Phys.* **2020**, *2*, 499−510.

(13) Al-Shidaifat, A.; Chakrabartty, S.; Kumar, S.; Acharjee, S.; Song, H. A novel characterization and performance measurement of memristor devices for synaptic emulators in advanced neuro-computing. *Micromachines* **2020**, *11*, 89.

(14) Chakraborty, I.; Jaiswal, A.; Saha, A.; Gupta, S.; Roy, K. Pathways to efficient neuromorphic computing with non-volatile memory technologies. *Applied Physics Reviews* **2020**, *7*, 021308.
(15) Sahu, M. C.; Jena, A. K.; Mallik, S. K.; Roy, S.; Sahoo, S.; Ajimsha, R. S.; Misra, P.; Sahoo, S. Reconfigurable low-power TiO2 memristor for integration of artificial synapse and nociceptor. *ACS Appl. Mater. Interfaces* **2023**, *15*, 25713−25725.
(16) Yu, Y.; Wang, C.; Wen, Y.; Jiang, C.; Abrahams, I.; Du, Z.; Sun, J.; Huang, X. Realization of volatile and non-volatile resistive switching with N-TiO_2 nanorod arrays based memristive devices through compositional control. *J. Alloys Compd.* **2022**, *909*, 164743.
(17) Chekol, S. A.; Menzel, S.; Ahmad, R. W.; Waser, R.; Hoffmann-Eifert, S. Effect of the threshold kinetics on the filament relaxation behavior of Ag-based diffusive memristors. *Adv. Funct. Mater.* **2022**, *32*, 1−11.
(18) Chen, S.; Mahmoodi, M. R.; Shi, Y.; Mahata, C.; Yuan, B.; Liang, X.; Wen, C.; Hui, F.; Akinwande, D.; Strukov, D. B.; Lanza, M. Wafer-scale integration of two-dimensional materials in high-density memristive crossbar arrays for artificial neural networks. *Nat. Electron.* **2020**, *3*, 638−645.
(19) Jena, A. K.; Sahu, M. C.; Mohanan, K. U.; Mallik, S. K.; Sahoo, S.; Pradhan, G. K.; Sahoo, S. Bipolar resistive switching in TiO_2 artificial synapse mimicking pavlov's associative learning. *ACS Appl. Mater. Interfaces* **2023**, *15*, 3574−3585.
(20) Jang, J. T.; Min, J.; Kim, D.; Park, J.; Choi, S. J.; Kim, D. M.; Cho, S.; Kim, D. H. A highly reliable physics-based spice compact model of IGZO memristor considering the dependence on electrode metals and deposition sequence. *Solid-State Electron.* **2020**, *166*, 107764.
(21) Jang, J. T.; Min, J.; Hwang, Y.; Choi, S.-J.; Kim, D. M.; Kim, H.; Kim, D. H. Digital and analog switching characteristics of ingazno memristor depending on top electrode material for neuromorphic system. *IEEE Access* **2020**, *8*, 192304−192311.
(22) Pabst, O.; Tronstad, C.; Martinsen, O. G. Ieee, Instrumentation, electrode choice and challenges in human skin memristor measurement, in: *39th Annual International Conference of the IEEE-Engineering-in-Medicine-and-Biology-Society (EMBC)*; IEEE: South Korea, 2017; pp 1844−1848.
(23) Gale, E.; Pearson, D.; Kitson, S.; Adamatzky, A.; de Lacy Costello, B. The effect of changing electrode metal on solution-processed flexible titanium dioxide memristors. *Mater. Chem. Phys.* **2015**, *162*, 20−30.
(24) Praveen, P.; Rose, T. P.; Saji, K. J. Top electrode dependent resistive switching in M/ZnO/ITO memristors, M = Al, ITO, Cu, and Au. *Microelectron. J.* **2022**, *121*, 105388.
(25) Yeon, H.; Lin, P.; Choi, C.; Tan, S. H.; Park, Y.; Lee, D.; Lee, J.; Xu, F.; Gao, B.; Wu, H.; Qian, H.; Nie, Y.; Kim, S.; Kim, J. Alloying conducting channels for reliable neuromorphic computing. *Nat. Nanotechnol.* **2020**, *15*, 574−579.
(26) Kumar, A.; Baghini, M. S. Experimental study for selection of electrode material for ZnO-based memristors. *Electron. Lett.* **2014**, *50*, 1547−1549.
(27) Ge, N.; Zhang, M. X.; Zhang, L.; Yang, J. J.; Li, Z.; Williams, R. S. Electrode-material dependent switching in TaO_x memristors. *Semicond. Sci. Technol.* **2014**, *29*, 104003.
(28) Shi, T.; Wang, R.; Wu, Z.; Sun, Y.; An, J.; Liu, Q. A Review of Resistive Switching Devices: Performance Improvement, Characterization, and Applications. *Appl. Sci. Converg. Technol.* **2021**, *2*, 2000109.
(29) Kang, S. M.; Choi, D.; Eshraghian, J. K.; Zhou, P.; Kim, J.; Kong, B.-S.; Zhu, X.; Demirkol, A. S.; Ascoli, A.; Tetzlaff, R.; Lu, W. D.; Chua, L. O. How to build a memristive integrate-and-fire model for spiking neuronal signal generation. *IEEE Trans. Circuits Syst.* **2021**, *68*, 4837−4850.
(30) Yao, P.; Wu, H.; Gao, B.; Tang, J.; Zhang, Q.; Zhang, W.; Yang, J. J.; Qian, H. Fully hardware-implemented memristor convolutional neural network. *Nature* **2020**, *577*, 641−646.
(31) Yang, Y.; Zhu, X.; Ma, Z.; Hu, H.; Chen, T.; Li, W.; Xu, J.; Xu, L.; Chen, K. Artificial HfO_2/TiO_x synapses with controllable memory window and high uniformity for brain-inspired computing. *Nanomaterials* **2023**, *13*, 605.
(32) Yu, Y. T.; Wang, C. Q.; Jiang, C.; Wang, L. Z.; Wang, Z.; Du, Z. J.; Sun, J.; Abrahams, I.; Huang, X. Z. Nitrogen-doped titanium dioxide nanorod array memristors with synaptic features and tunable memory lifetime for neuromorphic computing. *J. Alloys Compd.* **2021**, *868*, 159194.
(33) Fu, Y.; Dong, B.; Su, W. C.; Lin, C. Y.; Zhou, K. J.; Chang, T. C.; Zhuge, F.; Li, Y.; He, Y.; Gao, B.; Miao, X. S. Enhancing $LiAlO_X$ synaptic performance by reducing the schottky barrier height for deep neural network applications. *Nanoscale* **2020**, *12*, 22970−22977.
(34) Isyaku, U. B.; Khir, M. H. B.; Nawi, I. M.; Zakariya, M. A.; Zahoor, F. ZnO based resistive random access memory device: A prospective multifunctional next-generation memory. *IEEE Access* **2021**, *9*, 105012−105047.
(35) Ginnaram, S.; Qiu, J. T.; Maikap, S. Controlling Cu migration on resistive switching, artificial synapse, and glucose/saliva detection by using an optimized AlO_x interfacial layer in a-CO_x-based conductive bridge random access memory. *ACS Omega* **2020**, *5*, 7032−7043.
(36) Kwon, J.; Sharma, A. A.; Bain, J. A.; Picard, Y. N.; Skowronski, M. Oxygen vacancy creation, drift, and aggregation in TiO_2-based resistive switches at low temperature and voltage. *Adv. Funct. Mater.* **2015**, *25*, 2876−2883.
(37) Prezioso, M.; Merrikh-Bayat, F.; Hoskins, B. D.; Adam, G. C.; Likharev, K. K.; Strukov, D. B. Training and operation of an integrated neuromorphic network based on metal-oxide memristors. *Nature* **2015**, *521*, 61−64.
(38) Porro, S.; Jasmin, A.; Bejtka, K.; Conti, D.; Perrone, D.; Guastella, S.; Pirri, C. F.; Chiolerio, A.; Ricciardi, C. Low-temperature atomic layer deposition of TiO_2 thin layers for the processing of memristive devices. *J. Vac. Sci. Technol., A* **2016**, *34*, 01A147.
(39) Chauhan, M.; Choudhary, S.; Sharma, S. K. Reliable memristive switching empowered by Ag/NiO/W ReRAM configuration for multi-level non-volatile memory applications. *Adv. Electron. Mater.* **2024**, *10*, 1−11.
(40) Ebenhoch, C.; Schmidt-Mende, L. TiO_2 nanowire array memristive devices emulating functionalities of biological synapses. *Adv. Electron. Mater.* **2021**, *7*, 2000950.
(41) Kumar, A.; Das, M.; Mukherjee, S. Oxide based memristors: Fabrication, mechanism, and application. In *Reference Module in Materials Science and Materials Engineering*; Elsevier, 2018.
(42) Funck, C.; Menzel, S. Comprehensive model of electron conduction in oxide-based memristive devices. *ACS Appl. Electron. Mater.* **2021**, *3*, 3674−3692.
(43) Hu, S.; Yue, J.; Jiang, C.; Tang, X.; Huang, X.; Du, Z.; Wang, C. Resistive switching behavior and mechanism in flexible TiO_2@c_f memristor crossbars. *Ceram. Int.* **2019**, *45*, 10182−10186.
(44) Khisamov, R. K.; Khalikova, G. R.; Kistanov, A. A.; Korznikova, G. F.; Korznikova, E. A.; Nazarov, K. S.; Sergeev, S. N.; Shayakhmetov, R. U.; Timiryaev, R. R.; Yumaguzin, Y. M.; Mulyukov, R. R. Microstructure, microhardness and work function of in-situ Al-Cu composite processed by mechanical alloying by means of high-pressure torsion. *Continuum Mech. Therm.* **2023**, *35*, 1433−1444.
(45) Kim, K.; Lim, J. G.; Hu, S. M.; Jeong, Y.; Kim, J.; Lee, S.; Kwak, J. Y.; Park, J.; Hwang, G. W.; Lee, K.-S.; Park, S.; Lee, W.-S.; Ju, B.-K.; Park, J. K.; Kim, I. Multifilamentary switching of Cu/SiOx memristive devices with a Ge-implanted a-Si underlayer for analog synaptic devices. *NPG Asia Mater.* **2023**, *15*, 48.
(46) Zhang, X. M.; Liu, S.; Zhao, X. L.; Wu, F. C.; Wu, Q. T.; Wang, W.; Cao, R. R.; Fang, Y. L.; Lv, H. B.; Long, S. B.; Liu, Q.; Liu, M. Emulating short-term and long-term plasticity of bio-synapse based on Cu/a-Si/Pt memristor. *IEEE Electron Device Lett.* **2017**, *38*, 1208−1211.
(47) Li, W.; Cochell, T.; Manthiram, A. Activation of aluminum as an effective reducing agent by pitting corrosion for wet-chemical synthesis. *Sci. Rep.* **2013**, *3*, 1229.

https://doi.org/10.1021/acsomega.4c00320
ACS Omega 2024, 9, 24601−24609

(48) Chen, K.; Xue, D. Reaction route to the crystallization of copper oxides. *Appl. Sci. Converg. Technol.* **2014**, *23*, 14−26.

https://doi.org/10.1021/acsomega.4c00320
ACS Omega 2024, 9, 24601−24609